Capturing transition features around a wing by reduced-order modeling based on compressible Navier-Stokes equations

Rémi Bourguet, Marianna Braza, Alain Sevrain, Abdelatif Bouhadji

Capturing transition features around a wing by reduced-order modeling based on compressible Navier–Stokes equations

Rémi Bourguet,[a] Marianna Braza, Alain Sévrain, and Abdellatif Bouhadji[b]
Institut de Mécanique des Fluides de Toulouse, 6 Allée du Professeur C. Soula, Toulouse 31400, France

The three-dimensional transition in the flow around a NACA0012 wing of constant spanwise section at Mach number 0.3, Reynolds number 800, and incidence 20° is investigated by direct numerical simulation and reduced-order modeling. The interaction between the von Kármán and the secondary instabilities is analyzed. Irregular events in the flow transition modulating the spanwise undulation are highlighted and quantified. These transition features, including "local intermittencies" in the secondary instability pattern, are efficiently captured by a reduced-order model derived by means of the Galerkin projection of the compressible flow Navier–Stokes equations onto a truncated proper orthogonal decomposition basis.

I. INTRODUCTION

In the context of complex aerodynamic flow prediction, the investigation of the transition to turbulence is a challenging issue, especially for design purposes. To this end, the direct numerical simulation (DNS) is a powerful approach for physical analysis of fundamental mechanisms of the flow transition that appear at low Reynolds number and that persist at high-Reynolds number regimes. The Reynolds number is defined as $\mathrm{Re}=\rho_\infty u_\infty c/\mu_\infty$, where ρ_∞, u_∞, and μ_∞ are fluid upstream density, velocity, and dynamic viscosity, respectively, and c is a characteristic length of the body, wing chord length in the present study. However, this approach demands a considerable number of degrees of freedom to capture the flow physics. This is also the case for the large eddy simulation (LES), as well as for hybrid (statistical-LES) turbulence modeling, to achieve prediction at high Re. Therefore, "physics-driven" reduced-order models (ROMs) are needed. The transition to turbulence around wings at high Re was analyzed by a great deal of works (e.g., Ref. 1), whereas it is less studied at low and moderate Re. The period-doubling mechanism in two-dimensional flows around a NACA0012 airfoil has been investigated in Ref. 2. In the incompressible case, the onset of the three-dimensional transition in the wake of a wing at high incidence has been studied in Ref. 3. The transition induced by compressibility effects in the high-transonic regime around a wing has been examined in two dimensions[4] and in three dimensions.[5] These studies quantified the predominant wavelengths concerning the von Kármán, shear layer, and secondary instabilities, and the last analyzed the nature of the secondary instability by a global oscillator model. These works reported the high complexity of the flow transition in the incompressible and in the high-transonic regimes. Therefore, in the present study, three-dimensional transition phenomena are examined at the onset of compressibility effects as well as the ability of ROM in estimating them appropriately.

During the past two decades, ROMs of low-Re periodic and transient wall flows have been developed by means of proper orthogonal decomposition (POD)-Galerkin approach (e.g., Refs. 6 and 7). Recent studies have proven the efficiency of such ROMs for the prediction of nearly periodic and more chaotic three-dimensional flows on the basis of DNS (Ref. 8) or LES,[9] for example, and for turbulent flow analysis and modeling.[10,11] However, the majority of ROMs focus on the incompressible Navier–Stokes equations and only few studies deal with compressible flows. Assuming isentropic conditions, ROMs for compressible cavity flows have been developed.[12] The difficulties induced by coupling thermodynamic and kinematic state variables in the compressible Navier–Stokes equations can be solved by considering an appropriate state formulation (Refs. 13 and 14, in two dimensions). In the present study, this formulation is utilized in the three-dimensional case and a consistent inner product is considered for POD. The present ROM efficiency is examined in respect of capturing three-dimensional transition features predicted by DNS, especially irregularities that appear in space-time evolution of flow quantities. This is a prerequisite before using ROM as a prediction tool for parametric studies within suitable confidence intervals. Section II briefly describes the numerical method. Section III focuses on DNS results. Section IV presents the ROM and results regarding its reliability.

II. NUMERICAL METHOD

The complete, time-dependent Navier–Stokes equations have been solved in three dimensions under a conservative form, in a general nonorthogonal curvilinear coordinate system. The ICARE/IMFT (Ref. 4) in-house finite volume software for compressible flows around bodies has been employed. The Roe upwind scheme[15] with monotonic upstream schemes for conservative laws (MUSCL) approach[16] has been used for convection and pressure terms. Diffusion terms have been discretized by central differences and temporal

[a]Present address: Massachusetts Institute of Technology, 77 Massachusetts Avenue, Cambridge, MA 02139, USA. Electronic mail: bourguet@mit.edu.
[b]Present address: Ballard Power Systems Inc., British Columbia, Canada.

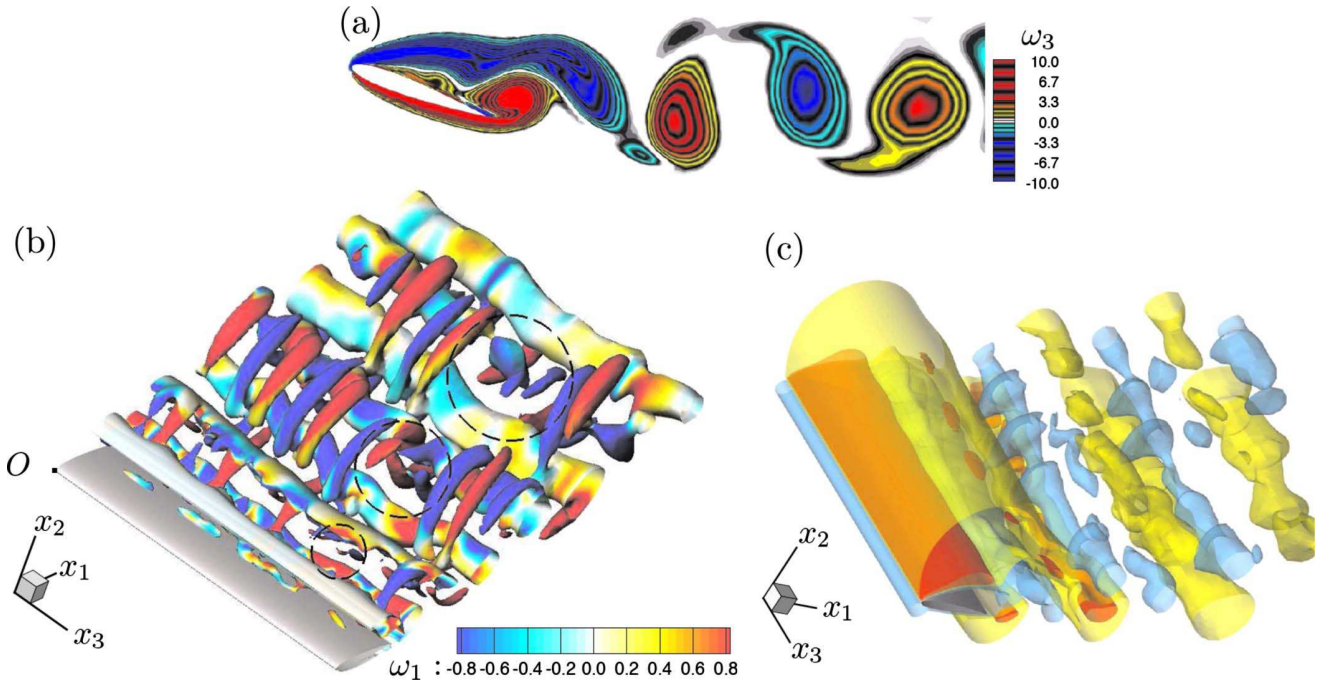

FIG. 1. (Color online) Instantaneous (a) isocontours of ω_3 vorticity component at $x_3/c=2$, (b) isosurface of Q criterion ($Q=0.3$) colored by isocontours of ω_1, and (c) isosurfaces of Mach number (Ma=0.21/0.32/0.39). Dashed circles indicate irregularities in spanwise pattern.

terms by an explicit four-stage Runge–Kutta scheme. Space and time schemes are second-order accurate. The computational domain is a C-type grid ($369\times89\times101$) of four chord lengths (c) in the spanwise direction, $7c$ from the trailing edge to the upstream outer boundary and $10c$ from the leading edge to the downstream outer boundary. The perfect gas equation is used as well as the Sutherland law to define the dynamic viscosity. The boundary conditions are no slip and constant temperature on the wing, the upstream flow temperature $T_\infty=300$ K, Mach number $\mathrm{Ma}=u_\infty/\sqrt{\gamma RT_\infty}=0.3$, where $\gamma=1.4$ is the polytropic coefficient and $R=287$ J kg^{-1} K^{-1} is the ideal gas constant, and Reynolds number Re=800. Free stream conditions have been imposed at the far field boundaries, except downstream of the wing at the outlet boundary, where a first-order extrapolation has been used for the unknown variables. Neumann-type boundary conditions have been imposed on the lateral boundaries of the computational domain at both ends of the wing in a spanwise direction. Detailed grid convergence and time-step studies have been previously performed in two and three dimensions to ensure the validity of the software, as well as numerical tests concerning the computational domain size.[4,17] Moreover, the flow has been slightly perturbed by a random field of small magnitude ($10^{-4}u_\infty$) introduced as free stream boundary condition for the transverse velocity component to shorten the transient phase toward appearance of the secondary instability. This technique had been verified in previous studies concerning similar flow configurations[3,18] where it was shown that the small perturbation magnitude has no effect on the final instability development beyond the transient phase. A two-dimensional simulation of the same flow has been carried out by using the same grid (369×89) in two dimensions.

III. THREE-DIMENSIONAL TRANSITION IN THE FLOW AROUND A WING

The flow around a NACA0012 wing at 20° of incidence in the above mentioned conditions exhibits a strong unsteady character induced by the interaction between two instability modes, the von Kármán and the secondary instabilities. The von Kármán instability induces a nearly periodic alternating leading/trailing edge vortex shedding illustrated in Fig. 1(a). The Strouhal number associated with the fundamental frequency of this instability has been evaluated on more than 40 vortex shedding events of the established three-dimensional flow and is found equal to 0.55. This is in good agreement with incompressible flow simulations.[3] The secondary instability appears as a large spanwise wavelength undulation of the von Kármán vortex rows, accompanied by "braidlike" structures of streamwise vorticity. This is illustrated in Fig. 1(b) by the isosurface of Q criterion.[19] The spanwise wavelength of the secondary instability is found in the range $\lambda_3/c\in[0.74,0.83]$. Considering an "equivalent bluff body" length scale defined as $l=c\sin(20°)$, comparison can be made with circular cylinder wake studies at equivalent Re $=800\sin(20°)=274$. The A- and B-mode transition patterns studied experimentally in Refs. 20 and 21 and numerically in Ref. 18, for example, are characterized by $\lambda_3/l\in[3,4]$ and $\lambda_3/l\approx1$ wavelengths, respectively. In the present study, the predicted wavelength $\lambda_3/l\in[2.2,2.4]$ could be related with the development of the C-mode pattern set forward in Ref.

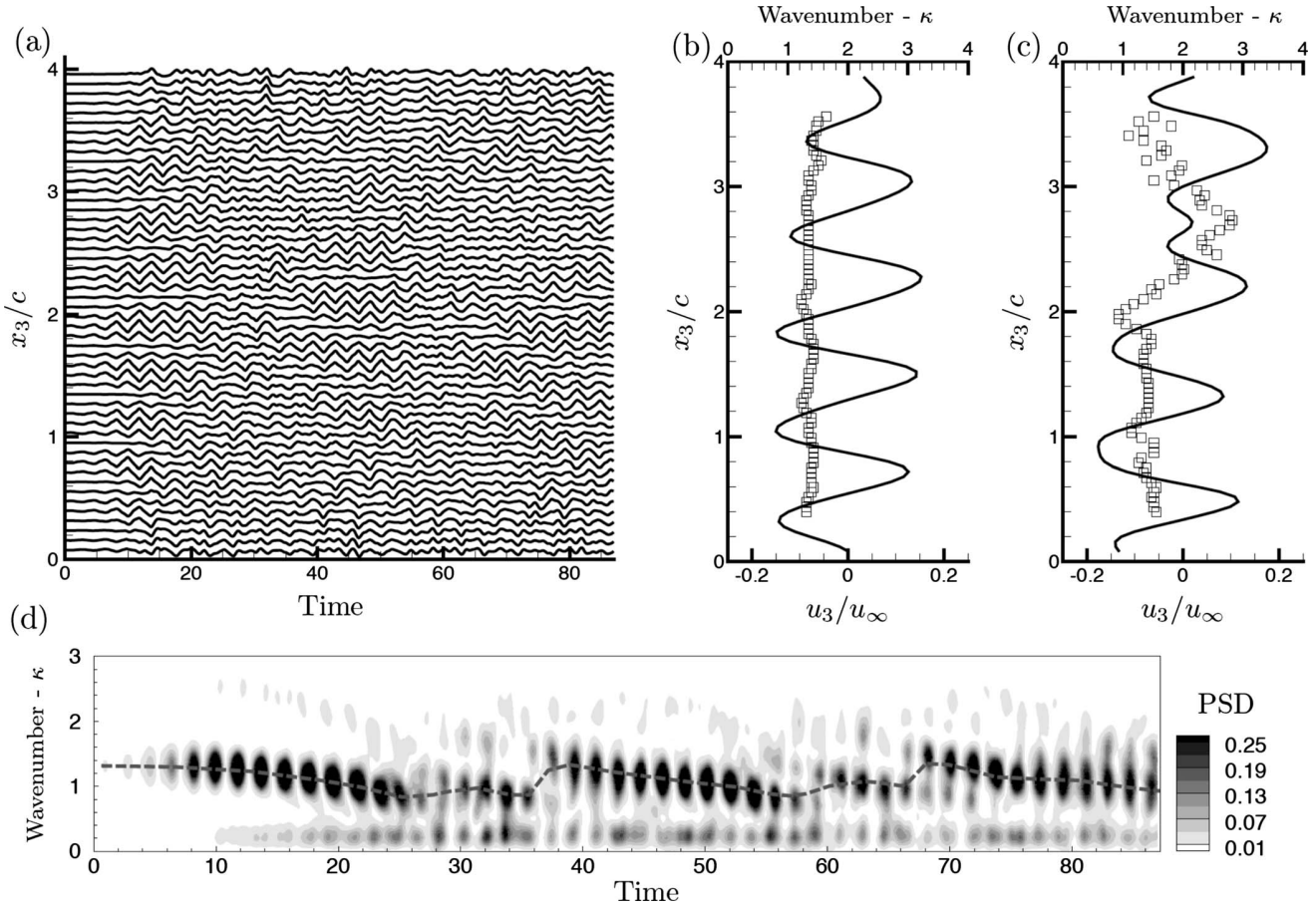

FIG. 2. (a) u_3 as a function of time in 50 spanwise positions ($x_1/c=0.71$, $x_2/c=0.16$). (b) u_3 as a function of x_3/c at $t=10.4$, same (x_1,x_2) location (plain lines); predominant wavenumber κ (squares). (c) Same as (b), $t=77.1$. (d) PSD of u_3 along the span as a function of time, same (x_1,x_2) location; predominant wavenumber κ' (dashed line).

22. The C-mode transition, which has been observed in wakes with forced asymmetry,[22] prescribed wavelength,[23] and which was examined by a three-dimensional Floquet analysis,[24,25] is characterized by an intermediate wavelength $\lambda_3/l\approx 2$. The significant decrease in the Strouhal number in the C-mode transition compared to two-dimensional case[22] has not been observed in the present study. Furthermore, Fig. 1(b) shows spanwise events that modify the secondary instability pattern, as described in the following.

The present aerodynamic lift (C_l) and drag (C_d) coefficients are close to those reported in Ref. 3. The time-averaged coefficients are $\overline{C_l}=0.90$ and $\overline{C_d}=0.45$ in two dimensions, $\overline{C_l}=0.85$ and $\overline{C_d}=0.43$ in three dimensions. As in case of previous DNS, a reduction in the time-averaged values and amplitudes of the lift and drag coefficients is observed between two- and three-dimensional simulations. The present results show that the main features of the flow configuration of interest are rather similar to lower Mach number flows. However, compressibility effects arise in the present case. In the acceleration region on the upper side of the wing, the Mach number equals 0.45 and the relative density variations in the field are higher than 20% of the upstream density.

Figure 1(b) shows chaotic states in the spanwise evolution of the vortex filaments that have not been observed in the incompressible case.[3] These consist of irregular appearance of "rarefied" spanwise regions, where one spanwise-periodic event is missing and an irregular vortex structure appears instead, breaking the continuous undulation of the von Kármán vortex rows [see indicated areas in Fig. 1(b)]. The present study aims at tracking these events and at quantifying their impact in the flow transition. Figure 1(c) shows isosurfaces of Mach number, also indicating an irregular spanwise undulation and wavelength dispersion. The above mentioned irregularities can be observed in the recirculation region at the upper side of the wing, as illustrated in Fig. 2(a). In this figure and in the following, time is nondimensionalized by chord length and upstream flow velocity. The monitoring starts after approximately 20 von Kármán vortex shedding events. In Figs. 2(b) and 2(c), instantaneous spanwise velocity profiles in the recirculation region are plotted. Space/frequency analysis is carried out on these signals to quantify the wavelength variation along the span. A spectral analysis is performed along the span by considering a sliding window of width $2\Delta x_3=0.8c$. The demodulated transverse velocity signal (u_3^d) is used to evaluate the predominant wavenumbers. The demodulated signal is defined by $u_3^d=u_3/A(u_3)$. The local amplitude $A(u_3)$ is estimated owing to the Hilbert transform $H(u_3)$ by $A(u_3)=|u_3+iH(u_3)|$. The

predominant maximum energy wavenumbers [squares in Figs. 2(b) and 2(c)] are plotted as functions of x_3/c. These are defined by $\kappa(x_3,t)=\arg\max_{\kappa_0\geq 0} P_{[x_3-\Delta x_3,x_3+\Delta x_3]}u_3^d(\cdot,t)\times(\kappa_0)$, where $P_{[a,b]}v(\cdot,t)$ denotes v spatial power spectrum density (PSD) evaluated on the segment $[a,b]$ along the span at time t. The Burg algorithm is applied for autoregressive PSD estimation.[26] A strong wavelength (phase) modulation occurs along the span, as well as a large variation of the velocity amplitude. In the region where the phase modulation appears, there is a significant increase of the wavenumber of the velocity signal related with irregular structure appearance. Figure 2(d) shows the temporal evolution of the spatial power spectrum of u_3 along the whole span within the recirculation region. The predominant wavenumber $\kappa'(t)=\arg\max_{\kappa_0\geq 0} P_{[0,4c]}u_3(\cdot,t)(\kappa_0)$ exhibits a significant variation as a function of time [qualitative plot, dashed line in Fig. 2(d)]. This is closely associated with the occurrence of phase and amplitude irregularities, as illustrated in Fig. 2(c). This phenomenon that appears randomly along the span in time and space is called here "intermittency," referring to the regular pattern of the secondary instability. Local irregularities can be associated with *A*-, *B*-, or *C*-mode transition in bluff body wakes. In particular, the vortex dislocation pattern[21] or vortex-adhesion point[22] consists of a junction of two adjacent von Kármán vortex rows, as mentioned also in the DNS study.[18] Moreover, in the incompressible case,[27] depicted a "losangelike" modulation of the spanwise vortices by using tomographic particle image velocimetry. The presently observed intermittencies have not been reported in the incompressible case concerning the same flow[3] and therefore are induced by flow compressibility. The origin of these irregular events could be investigated by using elliptic stability theory,[28] on a single undulated vortex row excited by small spanwise perturbations that could depend on Mach number. This kind of study is beyond the objectives of the present work that focuses on elaboration of a ROM, able to capture the onset of compressibility, the secondary instability, and the above mentioned intermittent irregularities.

IV. REDUCED-ORDER MODELING FOR COMPRESSIBLE FLOWS

The ROM is constructed by performing a Galerkin projection of the compressible Navier–Stokes equations onto a truncated POD basis. This needs an appropriate formulation of the flow quantities, as well as a suitable, dimensionally consistent, inner product for POD basis extraction, as explicited in the following. This method was previously used to derive ROM in the high-transonic regime.[14] The ROM approach relies on the assumption that the flow physics can be described by a reduced number of degrees of freedom. The present flow is governed by two main instabilities and shows a strong nearly periodic character induced by the von Kármán vortex shedding. Therefore this flow is, *a priori*, a good candidate for reduced-order representation. However, the flow transition is characterized by irregular events that are challenging to be captured by the low-dimensional approach. ROM method is detailed in Sec. IV A. ROM prediction results are reported and discussed in Sec. IV B.

A. Reduced-order modeling method

In this section, a dimensionally consistent definition of POD for compressible flows is set forward and the POD-Galerkin approach is applied to the fully compressible flow Navier–Stokes equations.

1. Proper orthogonal decomposition

In the context of model reduction, the POD is often used to extract the most energetic modes that are able to reconstruct the predominant flow structures. Assuming time-space separation, the POD consists in expanding the vector of state variables $\boldsymbol{v}$ as a linear combination of specific deterministic spatial eigenfunctions,[29]

$$\begin{aligned}\boldsymbol{v}(\boldsymbol{x},t)&=\overline{\boldsymbol{v}}(\boldsymbol{x})+\tilde{\boldsymbol{v}}(\boldsymbol{x},t)\\&=\overline{\boldsymbol{v}}(\boldsymbol{x})+\sum_{i=1}^{\infty}a_i(t)\boldsymbol{\Phi}_i(\boldsymbol{x})\approx\overline{\boldsymbol{v}}(\boldsymbol{x})+\sum_{i=1}^{N_{\mathrm{pod}}}a_i(t)\boldsymbol{\Phi}_i(\boldsymbol{x}).\end{aligned}\tag{1}$$

$\overline{\boldsymbol{v}}$ and $\tilde{\boldsymbol{v}}$ are the mean and fluctuating state vectors. The state formulation considered in the following is

$$\boldsymbol{v}=[1/\rho,u_1,u_2,u_3,p]^t.\tag{2}$$

ρ is the density, u_i are velocity components, and p is the pressure. The choice of this state formulation is justified in Sec. IV A 2. N_{pod} is the number of retained POD modes. a_i are time-dependent functions and $\boldsymbol{\Phi}_i$ are orthonormal spatial modes. These are the successive solutions of the following optimization problem:

$$\boldsymbol{\Phi}_{i+1}=\arg\max_{\boldsymbol{\Psi}\in L^2(\Omega)^d}\overline{(\tilde{\boldsymbol{v}}-\Pi_i\tilde{\boldsymbol{v}},\boldsymbol{\Psi})^2}\quad\text{with}\quad(\boldsymbol{\Psi},\boldsymbol{\Psi})=1.\tag{3}$$

The overline denotes time-averaging operator. $\Omega\subset\mathbb{R}^{d-2}$ is the spatial domain and d is the number of state variables ($d=5$ in the three-dimensional case). Π_i is the orthogonal projector onto the subspace spanned by the ith first modes. $(\cdot,\cdot)$ denotes the spatial inner product.

In the fully compressible case, the kinematic variables are associated with two thermodynamic quantities. A dimensionally consistent inner product is reached by a normalization of each state variable contribution as follows:

$$(\boldsymbol{v}^{\mathrm{I}},\boldsymbol{v}^{\mathrm{II}})=\sum_{n=1}^{d}\frac{1}{\sigma_n^2}\int_{\Omega}v_n^{\mathrm{I}}v_n^{\mathrm{II}}d\boldsymbol{x},\tag{4}$$

with

$$\sigma_n^2=\frac{1}{T_s}\int_{\Omega}\int_{t_0}^{t_0+T_s}\tilde{v}_n^2dtd\boldsymbol{x}.\tag{5}$$

$\boldsymbol{v}^{\mathrm{I}}$ and $\boldsymbol{v}^{\mathrm{II}}$ are two given states. σ_n^2 is the space-averaged variance of the nth variable and T_s is the time interval of the snapshot series. This inner product involves a systematic normalization procedure previously used in Ref. 30. This approach avoids dependency on a given nondimensional formulation of the governing equations. POD modes are determined by means of "snapshot-POD" technique.[31]

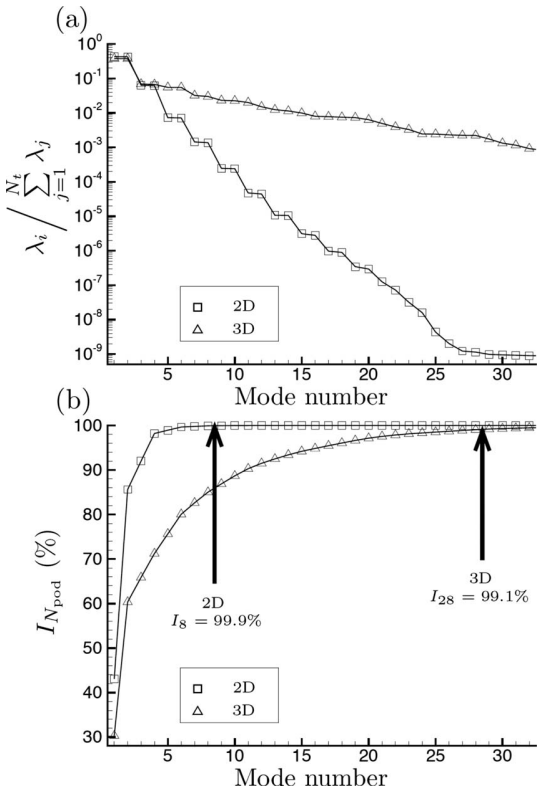

FIG. 3. (a) Relative statistical content of each POD mode, (b) relative statistical content of the truncated POD basis as a function of mode number, concerning the two- and three-dimensional snapshot series.

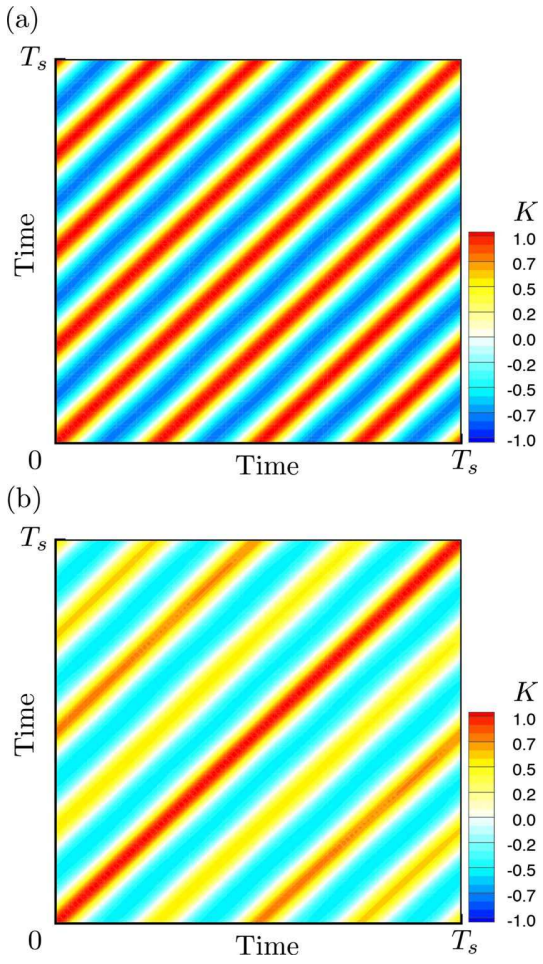

FIG. 4. (Color online) Normalized two-point temporal correlation matrices of the (a) two-dimensional and (b) three-dimensional flow simulations.

2. POD-Galerkin model

The compressible Navier–Stokes equations are expressed as quadratic fluxes by means of the previously defined state formulation (2), as reported in Ref. 13 for $i=1,2,3$,

$$\frac{\partial(1/\rho)}{\partial t} + u_\alpha \frac{\partial(1/\rho)}{\partial x_\alpha} - \frac{\partial u_\alpha}{\partial x_\alpha}(1/\rho) = 0,$$

$$\frac{\partial u_i}{\partial t} + u_\alpha \frac{\partial u_i}{\partial x_\alpha} + (1/\rho)\frac{\partial p}{\partial x_i} = (1/\rho)\frac{\partial \tau_{i\alpha}}{\partial x_\alpha}, \tag{6}$$

$$\frac{\partial p}{\partial t} + \gamma p \frac{\partial u_\alpha}{\partial x_\alpha} + u_\alpha \frac{\partial p}{\partial x_\alpha} = \frac{\gamma\mu}{\mathrm{Pr}} \frac{\partial^2 (p/\rho)}{\partial x_\alpha^2} + (\gamma - 1)\frac{\partial u_\alpha}{\partial x_\beta}\tau_{\alpha\beta},$$

where $\tau_{ij} = \mu(\partial u_i/\partial x_j + \partial u_j/\partial x_i - 2/3\,\partial u_\alpha/\partial x_\alpha \delta_{ij})$. Greek sub- and superscripts are used to specify implicit summations in previous expressions and in the following. μ is the fluid dynamic viscosity, Pr=0.72 is the Prandtl number, and δ_{ij} is the Kronecker symbol.

The Galerkin projection of the Navier–Stokes equations (6) onto the truncated POD basis yields the following quadratic polynomial ordinary differential equation (ODE) system, for $i=1,\ldots,N_{\rm pod}$:

$$\begin{aligned} \dot{a}_i &= (C_i + C_i^c) + \sum_{j=1}^{N_{\rm pod}} (L_{ij} + L_{ij}^c) a_j + \sum_{j,k=1}^{N_{\rm pod}} Q_{ijk} a_j a_k \\ &= f_i(\boldsymbol{C}^c, \boldsymbol{L}^c, \boldsymbol{a}), \\ a_i(t_0) &= (\boldsymbol{v}(\cdot,t_0) - \overline{\boldsymbol{v}}, \boldsymbol{\Phi}_i). \end{aligned} \tag{7}$$

C_i, L_{ij}, and Q_{ijk} coefficients are issued from the Galerkin projection while C_i^c and L_{ij}^c ones are additional calibration coefficients included to ensure ROM accuracy as detailed in the following. The constant coefficients issued from the Galerkin projection are computed as follows:

$$C_i = (\boldsymbol{F}_{11}^\alpha - \boldsymbol{A}_{11}^\alpha, \boldsymbol{\Phi}_i), \tag{8}$$

$$L_{ij} = (\boldsymbol{F}_{1(j+1)}^\alpha + \boldsymbol{F}_{(j+1)1}^\alpha - \boldsymbol{A}_{1(j+1)}^\alpha - \boldsymbol{A}_{(j+1)1}^\alpha, \boldsymbol{\Phi}_i), \tag{9}$$

$$Q_{ijk} = (\boldsymbol{F}_{(j+1)(k+1)}^\alpha - \boldsymbol{A}_{(j+1)(k+1)}^\alpha, \boldsymbol{\Phi}_i). \tag{10}$$

$\boldsymbol{A}_{jk}^i$ and $\boldsymbol{F}_{jk}^i$ terms involved in the implicit summations in Eqs. (8)–(10) are defined as follows: in the three-dimensional case,

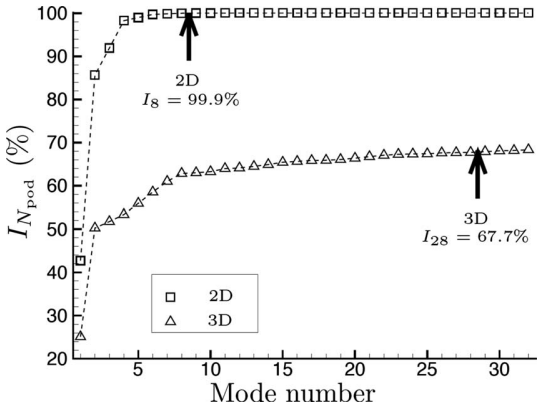

FIG. 5. Same as Fig. 3(b) for snapshot series beyond the time interval of the original snapshot series used to extract POD basis (over one von Kármán vortex shedding cycle).

$$\boldsymbol{A}^i_{jk} = \begin{bmatrix} \check{\Phi}^{u_i}_j \dfrac{\partial \check{\Phi}^{(1/\rho)}_k}{\partial x_i} - \check{\Phi}^{(1/\rho)}_j \dfrac{\partial \check{\Phi}^{u_i}_k}{\partial x_i} \\ \check{\Phi}^{u_i}_j \dfrac{\partial \check{\Phi}^{u_1}_k}{\partial x_i} + \check{\Phi}^{(1/\rho)}_j \dfrac{\partial \check{\Phi}^{p}_k}{\partial x_i} \delta_{1i} \\ \check{\Phi}^{u_i}_j \dfrac{\partial \check{\Phi}^{u_2}_k}{\partial x_i} + \check{\Phi}^{(1/\rho)}_j \dfrac{\partial \check{\Phi}^{p}_k}{\partial x_i} \delta_{2i} \\ \check{\Phi}^{u_i}_j \dfrac{\partial \check{\Phi}^{u_3}_k}{\partial x_i} + \check{\Phi}^{(1/\rho)}_j \dfrac{\partial \check{\Phi}^{p}_k}{\partial x_i} \delta_{3i} \\ \gamma \check{\Phi}^{p}_j \dfrac{\partial \check{\Phi}^{u_i}_k}{\partial x_i} + \check{\Phi}^{u_i}_j \dfrac{\partial \check{\Phi}^{p}_k}{\partial x_i} \end{bmatrix}, \tag{11}$$

$$\boldsymbol{F}^i_{jk} = \begin{bmatrix} 0 \\ \check{\Phi}^{(1/\rho)}_j \dfrac{\partial \check{\tau}_{1ik}}{\partial x_i} \\ \check{\Phi}^{(1/\rho)}_j \dfrac{\partial \check{\tau}_{2ik}}{\partial x_i} \\ \check{\Phi}^{(1/\rho)}_j \dfrac{\partial \check{\tau}_{3ik}}{\partial x_i} \\ \dfrac{\gamma\mu}{\mathrm{Pr}} \dfrac{\partial^2 \check{\Phi}^{p}_j \check{\Phi}^{(1/\rho)}_k}{\partial x_i^2} + (\gamma - 1) \dfrac{\partial \check{\Phi}^{u_\alpha}_j}{\partial x_i} \check{\tau}_{\alpha ik} \end{bmatrix}, \tag{12}$$

where $\check{\tau}_{ijk} = \mu(\partial \check{\Phi}^{u_i}_k / \partial x_j + \partial \check{\Phi}^{u_j}_k / \partial x_i - 2/3\, \partial \check{\Phi}^{u_\alpha}_k / \partial x_\alpha \delta_{ij})$ and $\check{\boldsymbol{\Phi}} = [\overline{\boldsymbol{v}}, \boldsymbol{\Phi}_1, \ldots, \boldsymbol{\Phi}_{N_{\rm pod}}]$. In the ROM, μ is assumed constant to allow evaluation of all the ODE coefficients, once for all.

As reported in Ref. 7, dynamical systems issued from the POD-Galerkin methodology can be structurally unstable and even tend to be so for oscillatory flows. To ensure ROM accuracy, different approaches have been envisaged in literature and especially calibration procedures (see, for example,

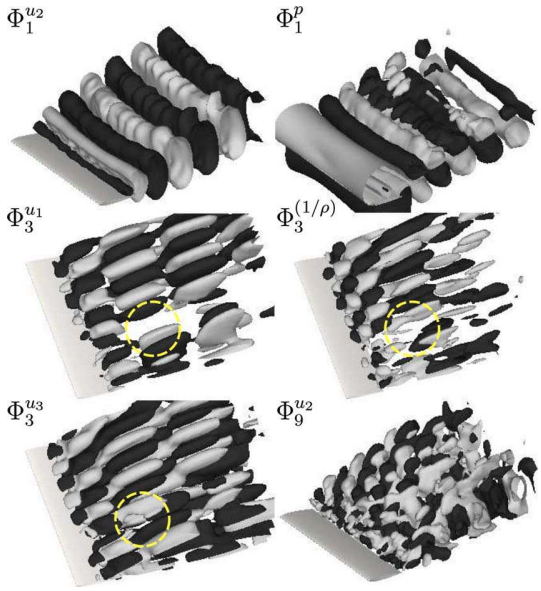

FIG. 6. (Color online) Selected POD mode isosurfaces, concerning the kinematic and thermodynamic quantities: $\Phi^{u_2}_1 = \pm 5.2$ m/s, $\Phi^{p}_1 = \pm 9.6 \times 10^{-3}$ Pa, $\Phi^{u_1}_3 = \pm 7.1$ m/s, $\Phi^{(1/\rho)}_3 = \pm 41$ m^3/kg, $\Phi^{u_3}_3 = \pm 3.5$ m/s, and $\Phi^{u_2}_9 = \pm 5.3$ m/s. Light/dark gray: positive/negative valued isosurfaces. Dashed circles indicate irregularities in spanwise pattern.

Ref. 32 for a review of ROM calibration approaches). A linearized calibration method is adopted here in a similar way to Ref. 9 in the incompressible case. This approach consists in minimizing ROM prediction error with respect to reference dynamics issued from the projection of DNS snapshots onto POD basis,

$$a^{\rm pod}_i = (\tilde{\boldsymbol{v}}, \boldsymbol{\Phi}_i), \tag{13}$$

while controlling calibration cost. The linearized prediction error is evaluated as

$$E(\boldsymbol{C}^c, \boldsymbol{L}^c) = \sum_{i=1}^{N_{\rm pod}} \int_{t_0}^{t_0+T_s} \left[a^{\rm pod}_i - a^{\rm pod}_i(t_0) - \int_{t_0}^{t} f_i(\boldsymbol{C}^c, \boldsymbol{L}^c, \boldsymbol{a}^{\rm pod}) dt' \right]^2 dt, \tag{14}$$

where f_i is the right-hand side of ROM (7). The error between reference dynamic derivatives and f_i, that is insensitive to accumulating phase errors, could also be envisaged for large integration periods. The following normalized error is considered in calibration procedure:

$$\mathcal{E}(\boldsymbol{C}^c, \boldsymbol{L}^c) = \frac{E(\boldsymbol{C}^c, \boldsymbol{L}^c)}{E(\boldsymbol{0}_{N_{\rm pod}}, \boldsymbol{0}_{N^2_{\rm pod}})}. \tag{15}$$

The calibration cost measures the weight of the calibration coefficients compared to those issued from the Galerkin projection [C_i and L_{ij} in Eq. (7)],

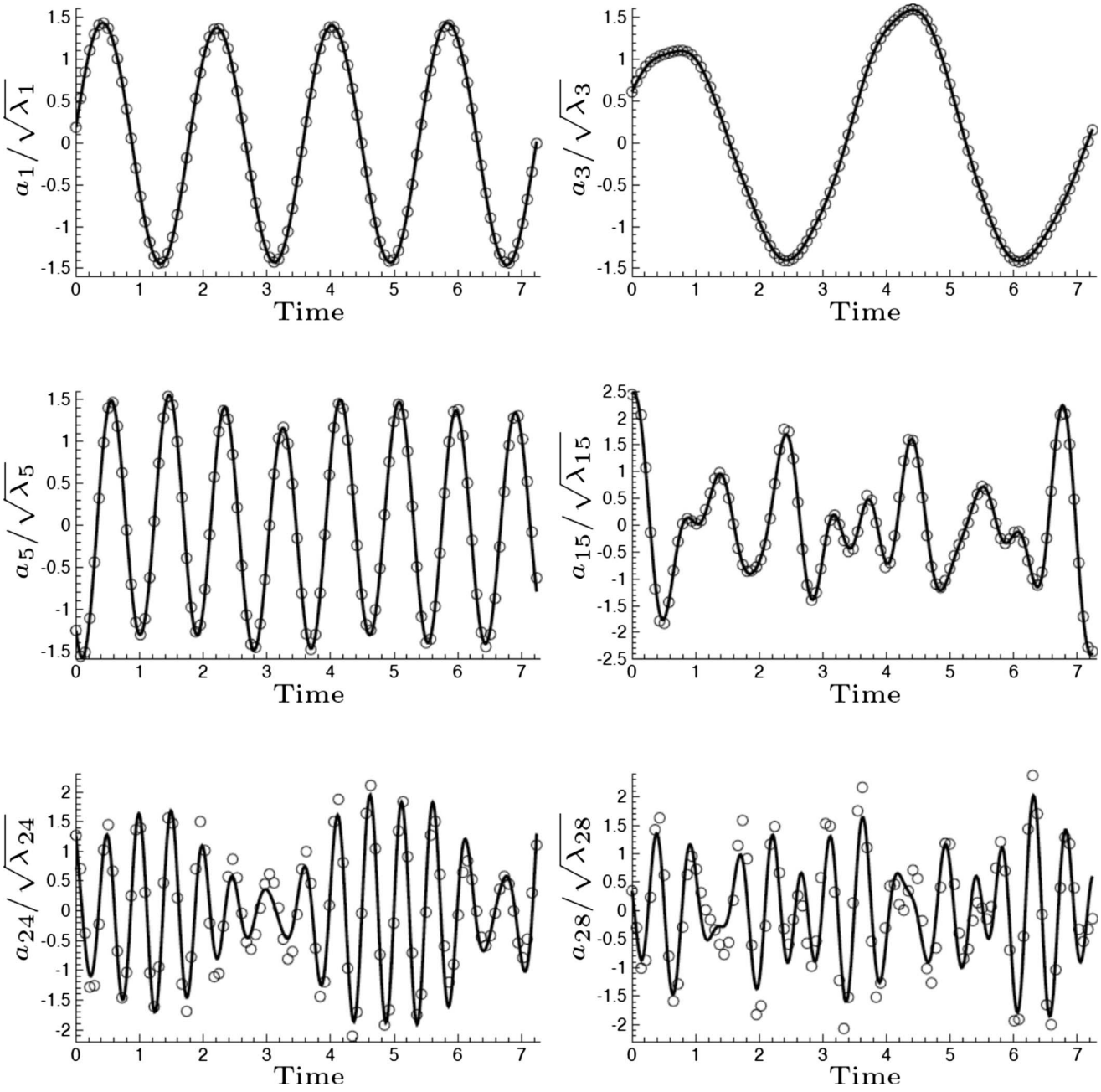

FIG. 7. Time-history of selected POD coefficients issued from: snapshot projection onto POD modes (a_i^{pod}, circles) and ROM integration (a_i^{rom}, plain lines), over four periods of the von Kármán vortex shedding (snapshots temporal horizon).

$$\mathcal{C}(\boldsymbol{C}^c,\boldsymbol{L}^c)=\frac{\|\boldsymbol{C}^c\|^2_{N_{\text{pod}}}+\|\boldsymbol{L}^c\|^2_{N^2_{\text{pod}}}}{\|\boldsymbol{C}\|^2_{N_{\text{pod}}}+\|\boldsymbol{L}\|^2_{N^2_{\text{pod}}}}. \tag{16}$$

The norms are defined by $\|\boldsymbol{C}\|^2_{N_{\text{pod}}}=C^2_\alpha$ and $\|\boldsymbol{L}\|^2_{N^2_{\text{pod}}}=L^2_{\alpha\beta}$.

The calibration coefficients C_i^c and L_{ij}^c in Eq. (7) are thus found by minimizing the following function that balances ROM prediction error and calibration cost by means of a blending coefficient $0<\theta<1$:

$$J(\boldsymbol{C}^c,\boldsymbol{L}^c,\theta)=\theta\mathcal{E}(\boldsymbol{C}^c,\boldsymbol{L}^c)+(1-\theta)\mathcal{C}(\boldsymbol{C}^c,\boldsymbol{L}^c). \tag{17}$$

Minimizing J is equivalent to solve N_{pod} linear systems of size $N_{\text{pod}}+1$. The blending coefficient θ can also be regarded as a regularization parameter in the Tikhonov regularization framework.[32,33] ROM integration is ensured by a fourth-order-accurate Runge–Kutta scheme.

B. ROM prediction

The time-dependent evolution of the flow transition in two and three dimensions is studied by considering two different series of flow fields containing $N_t=400$ snapshots each. These data sets correspond to four periods of the established von Kármán vortex shedding. This time interval (T_s) is considered for both ROM calibration and integration. The relative statistical content of each POD mode extracted

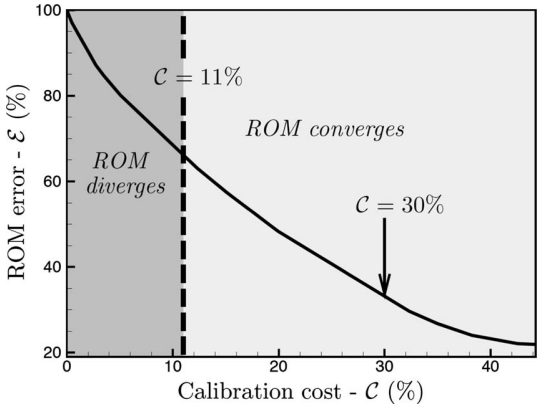

FIG. 8. ROM linearized prediction error as a function of the calibration cost in the three-dimensional case. The bold dashed line represents ROM convergence threshold. The arrow indicates the retained calibration cost.

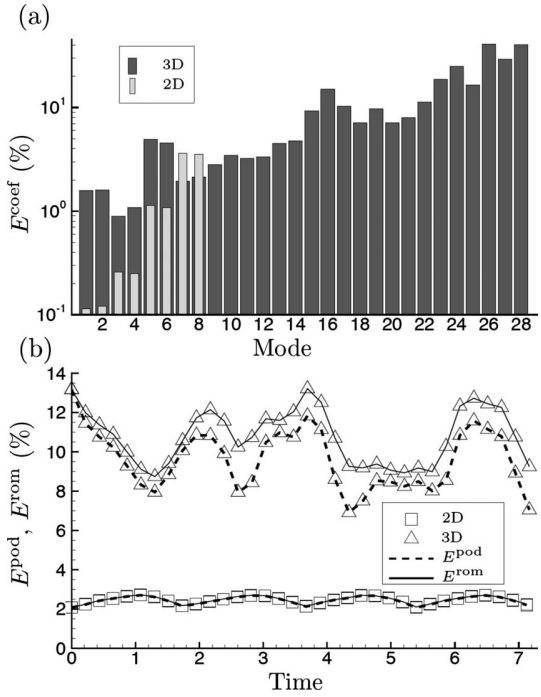

FIG. 9. Relative L^2 prediction errors of (a) POD time-dependent coefficients for each mode and (b) state vector fluctuations as a function of time, over the time interval of the snapshot series. In (b), both POD basis truncation and ROM errors are plotted.

from these snapshot series is measured by the relative magnitude of the corresponding eigenvalue λ_i of the time/space two-point correlation matrix, with $\lambda_{N_t}=0$. This is shown in Fig. 3, as well as the cumulative statistical content conveyed by the POD basis, defined by

$$I_{N_{\text{pod}}}=\frac{\Sigma_{i=1}^{N_{\text{pod}}}\lambda_i}{\Sigma_{i=1}^{N_t}\lambda_i}. \tag{18}$$

In Fig. 3(a), the first eigenvalues exhibit a pairwise coupling as previously reported in Refs. 8 and 7 for periodic flows. Because of the present flow nearly periodic character, the eigenfunctions of the temporal correlation matrix are close to real Fourier modes whose eigenvalues are pairwise equal. The flow nearly periodic character is illustrated by normalized temporal correlation matrices $K(t,t')=(\tilde{\boldsymbol{v}}(\cdot,t),\tilde{\boldsymbol{v}}(\cdot,t'))/\|\tilde{\boldsymbol{v}}(\cdot,t)\|\|\tilde{\boldsymbol{v}}(\cdot,t')\|$ in Fig. 4. The pairwise coupling of the eigenvalues is less pronounced in the three-dimensional flow that exhibits aperiodic events. Most of the dynamic system statistical content is represented by the first POD modes in both two- and three-dimensional cases. However, Fig. 3 shows that the three-dimensional flow, which involves complex instability interactions compared to the two-dimensional one, requires more POD modes for the same $I_{N_{\text{pod}}}$ (representation quality). $I_{N_{\text{pod}}}=99\%$ is chosen as a truncation criterion in the three-dimensional case and thus 28 modes are retained. For the two-dimensional flow, an eight-dimensional POD basis is considered.

The statistical content captured by the present POD basis beyond original snapshot series ($t>t_0+T_s$) is quantified (Fig. 5). This is measured by

$$I_{N_{\text{pod}}}=\frac{1}{T_a d}\sum_{i=1}^{N_{\text{pod}}}\int_{t_0+T_s}^{t_0+T_s+T_a}(\boldsymbol{v}^a-\overline{\boldsymbol{v}},\boldsymbol{\Phi}_i)^2 dt \tag{19}$$

since $\overline{\|\tilde{\boldsymbol{v}}\|^2}=d$ for the original snapshot series if inner product (4) is considered to define the norm. T_a is the time interval of the new snapshot series (one von Kármán vortex shedding cycle) and $\boldsymbol{v}^a$ are the new snapshots. A significant reduction in POD basis efficiency/relevance (≈30%) is observed in the three-dimensional case whereas the statistical content conveyed by the two-dimensional POD basis remains the same because of the strictly periodic character of the two-dimensional flow [Fig. 4(a)]. In the three-dimensional case, this reduction is related to the appearance of the previously mentioned aperiodic events. Considering this fact, ROM efficiency is examined over the original snapshots temporal horizon ($[t_0,t_0+T_s]$) in the present study.

Selected three-dimensional spatial POD modes are shown in Fig. 6. Although they do not correspond to coherent structures, the three-dimensional POD modes efficiently identify the von Kármán and the secondary instabilities, in the present case. The first pair combination in the flow-field reconstruction yields the alternating vortex pattern. However, this vortex pattern is highly modulated in the three-dimensional case. This modulation is captured by the higher-order modes, as shown in Fig. 6. For example, mode 3 is related to the reconstruction of the secondary instability. This mode clearly exhibits a local modification of the spanwise pattern where intermittency of the secondary instability occurs, as discussed in Sec. III (see indicated areas in Fig. 6). Higher-order modes present less organized patterns and can be associated with more chaotic phenomena related to the interaction between the two instability modes.

The time histories of selected POD reference coefficients a_i^{pod} (13) are shown in Fig. 7. As expected, the first POD

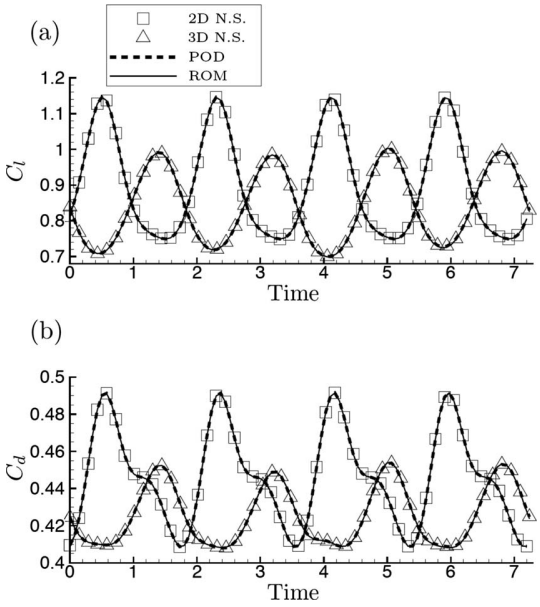

FIG. 10. Unsteady aerodynamic (a) lift and (b) drag coefficients issued from DNS, truncated POD basis representation, and ROM, as functions of time.

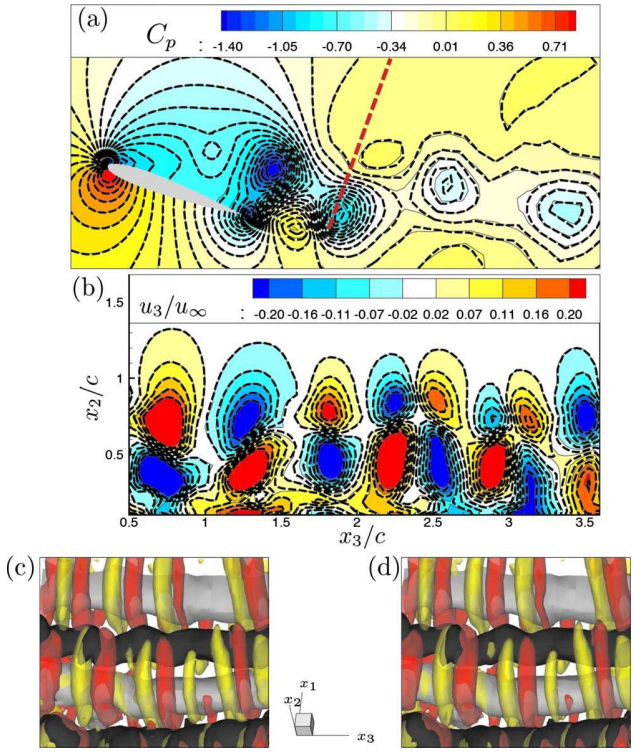

FIG. 11. (Color online) Instantaneous isocontours at final ROM integration time (t=7.239): (a) the pressure coefficient at x_3/c=2, (b) the transverse velocity component at x_1/c=1.5 [(x_3,x_2) plane]. Red dashed line in (a): location of plane (x_3,x_2) in (b). DNS: plain isolines and isocolor contours. ROM: dashed isolines. Instantaneous isosurfaces of ω_3=−1/1 and ω_2 =−0.5/0.5 in the wake, at final ROM integration time (t=7.239). (c) DNS; (d) ROM.

coefficients are close to periodic while higher-order ones are not. The coefficients associated with the secondary instability (modes 3 and 4) are approximately periodic at half frequency compared to the von Kármán instability. The higher-order coefficients display significant amplitude and frequency modulations.

While the uncalibrated three-dimensional ROM diverges after approximately 1.5 vortex shedding periods, convergence and satisfactory prediction are reached over the snapshots' temporal horizon for the calibration cost $\mathcal{C}$=11%. The uncalibrated two-dimensional ROM yields qualitatively correct prediction over the four vortex shedding cycles. In the following, a calibration cost threshold $\mathcal{C}$=30% is arbitrarily chosen for both two- and three-dimensional ROMs. Calibration diagram showing ROM linearized prediction error $\mathcal{E}$ (15) as a function of the calibration cost $\mathcal{C}$ (16) in the three-dimensional case is presented in Fig. 8.

As shown in Fig. 7 for the three-dimensional flow, the calibrated ROM achieves prediction of the POD time-dependent coefficients that provide an efficient flow reconstruction even in case of nonperiodic evolutions, as detailed at the end of the present section.

The relative L^2 prediction error of the temporal coefficients is defined by

$$E^{\mathrm{coef}}(i)=\sqrt{\frac{\overline{(a_i^{\mathrm{pod}}-a_i^{\mathrm{rom}})^2}}{\overline{(a_i^{\mathrm{pod}})^2}}}, \tag{20}$$

where a_i^{rom} are issued from ROM (7) integration. This error remains small even for the higher order modes [Fig. 9(a)]. The accuracy of the ROM is confirmed by the low values of the state vector prediction error over the entire spatial domain [Fig. 9(b)]. POD and ROM errors are defined by $E^{\mathrm{pod}}(t)=e(\boldsymbol{a}^{\mathrm{pod}},t)$ and $E^{\mathrm{rom}}(t)=e(\boldsymbol{a}^{\mathrm{rom}},t)$, respectively, where

$$e(\boldsymbol{a},t)=\frac{\left\|\tilde{\boldsymbol{v}}(\cdot,t)-\Sigma_{i=1}^{N_{\mathrm{pod}}}a_i(t)\boldsymbol{\Phi}_i\right\|}{\left\|\tilde{\boldsymbol{v}}(\cdot,t)\right\|}. \tag{21}$$

The difference between ROM and POD errors is very small. This means that the major part of the ROM error with respect to "high-fidelity" results is induced by the POD basis truncation in both two- and three-dimensional cases.

The instantaneous aerodynamic coefficients can be determined from the state vector predicted by the ROM since the state vector includes both kinematic and thermodynamic variables. These coefficients present a good comparison with those predicted by DNS (Fig. 10). This is an interesting aspect concerning the use of ROM in design procedures. Instantaneous flow fields issued from DNS and ROM are compared at the final ROM integration time (last snapshot) in Fig. 11. The pressure coefficient is accurately estimated by the present reduced-order approach [Fig. 11(a)]. Moreover, the spanwise pattern including irregularities of the secondary instability is well captured [Figs. 11(b)–11(d)].

V. CONCLUSION

The three-dimensional transition in the flow around a NACA0012 wing of constant spanwise section, at low Mach number and high incidence, has been investigated. The appearance of preferential wavenumbers due to the von Kármán and secondary instabilities has been analyzed. Intermittent modulations of the secondary instability have been identified and quantified. The transition process has been captured by an appropriate ROM derived from the compressible flow Navier–Stokes equations by means of the POD-Galerkin approach.

A consistent inner product has been set forward for POD in compressible flow context where kinematic and thermodynamic variables are coupled. A specific state formulation allowed to derive, by Galerkin projection of the high-fidelity model onto POD basis, a low-dimensional nonlinear ODE system relevant to the prediction of main flow features. ROM accuracy was ensured by a suitable calibration procedure balancing ROM ability in simulating reference flow previously resolved by DNS and respect of the high-fidelity model.

The present ROM provides an efficient simulation of both kinematic and thermodynamic quantities. In particular, an accurate prediction of the irregular events occurring in the secondary instability pattern was achieved considering a strongly reduced number of degrees of freedom compared to DNS. ROM reliability has been assessed for flows previously resolved by DNS, with an emphasis on the capture of deviations from periodicity. Therefore, this study demonstrates the relevance of the POD-Galerkin approach for low-dimensional modeling of the transition to turbulence in the flow around a wing at the onset of compressibility.

A prospect of the present work is the investigation of ROM reliability beyond snapshots and calibration temporal horizon and for the prediction of flows not previously simulated by DNS. In this context, low-dimensional models are generally not expected to predict exactly all erratic perturbations about dominant flow features and in that case, a further reduction in the number of degrees of freedom could be envisaged in the present model toward least-order modeling. In the domain of applications, ROM can be regarded as a powerful "physics-based" interpolator for parametric studies in optimal shape design, for example, as well as a key enabler for multiphysics simulations, especially in fluid-structure interaction.

ACKNOWLEDGMENTS

Calculations were performed at the Institut du Développement et des Ressources en Informatique Scientifique (IDRIS) and the Centre Informatique National de l'Enseignement Supérieur (CINES). Alain Dervieux is gratefully acknowledged for fruitful and stimulating discussions. The authors thank the referees for their helpful suggestions.

[1] D. Arnal, "Boundary-layer transition: Prediction, application to drag reduction," in Special Course on Skin Friction Drag Reduction, AGARD Technical Report No. 786, Loughton, Essex, 1992.

[2] T. H. Pulliam and J. A. Vastano, "Transition to chaos in an open unforced 2D flow," J. Comput. Phys. **105**, 133 (1993).

[3] Y. Hoarau, M. Braza, Y. Ventikos, D. Faghani, and G. Tzabiras, "Organized modes and the three-dimensional transition to turbulence in the incompressible flow around a NACA0012 wing," J. Fluid Mech. **496**, 63 (2003).

[4] A. Bouhadji and M. Braza, "Organised modes and shock-vortex interaction in unsteady viscous transonic flows around an aerofoil. Part I," Comput. Fluids **32**, 1233 (2003).

[5] S. Bourdet, A. Bouhadji, M. Braza, and F. Thiele, ""Direct numerical simulation of the three-dimensional transition to turbulence in the transonic flow around a wing," Flow, Turbul Combust. **71**, 203 (2003).

[6] A. Deane, I. Kevrekidis, G. E. Karniadakis, and S. Orszag, "Low-dimensional models for complex geometry flows: Application to grooved channels and circular cylinders," Phys. Fluids A **3**, 2337 (1991).

[7] B. R. Noack, K. Afanasiev, M. Morzynski, G. Tadmor, and F. Thiele, "A hierarchy of low-dimensional models for the transient and post-transient cylinder wake," J. Fluid Mech. **497**, 335 (2003).

[8] X. Ma and G. E. Karniadakis, "A low-dimensional model for simulating three-dimensional cylinder flow," J. Fluid Mech. **458**, 181 (2002).

[9] M. Couplet, C. Basdevant, and P. Sagaut, "Calibrated reduced-order POD-Galerkin system for fluid flow modelling," J. Comput. Phys. **207**, 192 (2005).

[10] B. R. Noack, M. Schlegel, B. Ahlborn, G. Mutschke, M. Morzyński, P. Comte, and G. Tadmor, ""A finite-time thermodynamics of unsteady fluid flows," J. Non-Equilib. Thermodyn. **33**, 103 (2008).

[11] D. M. Luchtenburg, B. Günter, B. R. Noack, R. King, and G. Tadmor, "A generalized mean-field model of the natural and high-frequency actuated flow around a high-lift configuration," J. Fluid Mech. **623**, 283 (2009).

[12] C. W. Rowley, T. Colonius, and R. M. Murray, "Model reduction for compressible flows using POD and Galerkin projection," Physica D **189**, 115 (2004).

[13] G. Vigo, A. Dervieux, M. Mallet, M. Ravachol, and B. Stoufflet, "Extension of methods based on the proper orthogonal decomposition to the simulation of unsteady compressible Navier-Stokes flows," *CFD'98, Proceedings of the Fourth ECCOMAS Conference* (Wiley, New York, 1998), pp. 648–653.

[14] R. Bourguet, M. Braza, and A. Dervieux, "Reduced-order modeling for unsteady transonic flows around an airfoil," Phys. Fluids **19**, 111704 (2007).

[15] P. L. Roe, "Approximate Riemann solvers, parameter vectors, and difference schemes," J. Comput. Phys. **43**, 357 (1981).

[16] B. van Leer, "Towards the ultimate conservative difference scheme. V. A second-order sequel to Godunov's method," J. Comput. Phys. **32**, 101 (1979).

[17] A. Bouhadji, "Analyse physique par simulation numérique de phénomènes de transition bi-et tridimensionnels dans l'écoulement compressible, visqueux autour d'une aile d'avion," Ph.D. thesis, Institut National Polytechnique de Toulouse, 1998.

[18] M. Braza, D. Faghani, and H. Persillon, "Successive stages and the role of natural vortex dislocations in three-dimensional wake transition," J. Fluid Mech. **439**, 1 (2001).

[19] J. C. R. Hunt, A. Wray, and P. Moin, "Eddies, stream, and convergence zones in turbulent flows," Center for Turbulence Research Report No. S88, 1988.

[20] C. H. K. Williamson, "The existence of two stages in the transition to three-dimensionality of a cylinder wake," Phys. Fluids **31**, 3165 (1988).

[21] C. H. K. Williamson, "The natural and forced formation of spot-like vortex dislocations in the transition of a wake," J. Fluid Mech. **243**, 393 (1992).

[22] H.-Q. Zhang, U. Fey, B. R. Noack, M. König, and H. Eckelmann, "On the transition of the cylinder wake," Phys. Fluids **7**, 779 (1995).

[23] G. E. Karniadakis and G. S. Triantafyllou, "Three-dimensional dynamics and transition to turbulence in the wake of bluff objects," J. Fluid Mech. **238**, 1 (1992).

[24] G. J. Sheard, M. C. Thompson, and K. Hourigan, "From spheres to circular cylinders: The stability and flow structures of bluff ring wakes," J. Fluid Mech. **492**, 147 (2003).

[25] G. J. Sheard, M. C. Thompson, and K. Hourigan, "Subharmonic mechanism of the mode C instability," Phys. Fluids **111702**, 1 (2005).

[26] S. L. Marple, *Digital Spectral Analysis* (Prentice-Hall, Englewood Cliffs, 1987).

[27] F. Scarano, C. Poelma, and J. Westerweel, Proceedings of the Seventh International Symposium on PIV, Rome, Italy, 2007, pp. 1–14.

[28]F. Waleffe, "On the three-dimensional instability of strained vortices," Phys. Fluids A **2**, 76 (1990).
[29]G. Berkooz, P. Holmes, and J. L. Lumley, "The proper orthogonal decomposition in the analysis of turbulent flows," Annu. Rev. Fluid Mech. **25**, 539 (1993).
[30]J. L. Lumley and A. Poje, "Low-dimensional models for flows with density fluctuations," Phys. Fluids **9**, 2023 (1997).
[31]L. Sirovich, "Turbulence and the dynamics of coherent structures. Part I-III," Q. Appl. Math. **45**, 561 (1987).
[32]L. Cordier, B. Abou El Majd, and J. Favier, "Calibration of POD reduced-order models by Tikhonov regularization," Int. J. Numer. Methods Fluids (in press).
[33]A. N. Tikhonov and V. A. Arsenin, *Solutions of Ill-Posed Problems* (Winston, Washington, 1977).